Long-range directional routing and spatial selection of high spin-purity valley trion emission in monolayer WS_2

Pei-Gang Chen, Zhiyong Li, Yun Qi, Tsz Wing Lo, Shubo Wang, Wei Jin, Shanhui Fan, Anatoly V. Zayats, and Dangyuan Lei*

Pei-Gang Chen - Department of Materials Science and Engineering, The City University of Hong Kong, Hong Kong 999077, China

Zhiyong Li - Department of Applied Biology and Chemical Technology, The Hong Kong Polytechnic University, Hong Kong 999077, China

Yun Qi - Department of Electrical Engineering, The Hong Kong Polytechnic University, Hong Kong 999077, China

Tsz Wing Lo - Department of Materials Science and Engineering, The City University of Hong Kong, Hong Kong 999077, China

Shubo Wang - Department of Physics, City University of Hong Kong, Hong Kong 999077, China

Wei Jin - Department of Electrical Engineering, The Hong Kong Polytechnic University, Hong Kong 999077, China

Shanhui Fan - Department of Electrical Engineering and Ginzton Laboratory, Stanford University, Stanford, CA 94305-4088, USA

Anatoly V. Zayats - Department of Physics and London Centre for Nanotechnology, King's College London, Strand, London, WC2R 2LS, UK

Dangyuan Lei - Department of Materials Science and Engineering, The City University of Hong Kong, Hong Kong 999077, China

KEYWORDS: TMDCs, valley trions emission, valley polarization, photonic spin-orbit interaction, microfiber, unidirectional transport

ABSTRACT: Valley-dependent excitation and emission in transition metal dichalcogenides (TMDCs) have recently emerged as a new avenue for optical data manipulation, quantum optical technologies and chiral photonics. The valley-polarized electronic states can be optically addressed through photonic spin-orbit interaction of excitonic emission, typically with plasmonic nanostructures, but their performance is limited by the low quantum yield of neutral excitons in TMDC multilayers and the large Ohmic loss of plasmonic systems. Here we demonstrate a valleytronic system based on the trion emission in high quantum yield WS_2 monolayers chirally coupled to a low-loss microfiber. The integrated system uses the spin properties of the waveguided modes to achieve long-range directional routing of valley excitations and also provides new opportunities to selectively address valley-dependent emission from different spatial locations around the microfiber. This valleytronic interface can be integrated with fiber communication devices and could open up an avenue for merging valley polarization and chiral photonics to uncover new mechanisms for optical information transport and manipulation in classical and quantum regimes.

Valleytronics has recently emerged as a promising direction for optical information processing in classical and quantum domains. It exploits valley pseudospins—the degenerate yet inequivalent energy extrema (i.e. valleys) in the electronic band structure of materials—to encode, process and store information. Valley pseudospins provide an additional degree of freedom that can be manipulated and detected by external physical fields such as static electric field and light.[1–6] A prominent class of materials for valleytronics implementations are the two-dimensional (2D) transition metal dichalcogenide (TMDC) materials, such as MoS_2, $MoSe_2$, WS_2, and WSe_2. These materials have drawn much attention since their atomically thin crystalline layers are subject to intense quantum confinement and reduced dielectric screening. In 2D TMDCs, the valley pseudospins at corners of the Brillouin zone are readily manipulated by coupling with the spin angular momentum (SAM) of light, dictated by valley-dependent optical selection rules. It is possible to selectively excite neutral excitons, charged trions or neutral biexcitons in chosen valleys using near-resonant circularly polarized excitation with appropriate optical SAM. These excitonic quasiparticles may recombine radiatively with emission of photons with optical spin handedness determined by the valley.[7–11] This SAM sensitivity allows optical manipulation of valley-related processes. Interfacing valley emission with various kinds of waveguides may lead to integrated photonic solutions for quantum optical technologies, chiral nanophotonics and optical data manipulation.[12–17]

Hybrid TMDC-nanophotonic systems were proposed as an effective platform for achieving valley-selective optical interactions.[18] Such systems rely on optical spin properties of guided modes. Optical SAM arises in both free space beams with circular polarization, where it is oriented along the wavevector (longitudinal spin), and guided waves, where evanescent field has spin perpendicular to the direction of propagation (transverse spin).[19,20] In the latter case, the spin-momentum locking completely determines the direction of propagation for a given spin direction, through photonic spin-orbit coupling.[21–25] This allows directional transport of circularly polarized photons emitted from different valleys by coupling spin-momentum-locked photonic modes with valley excitons.[18] This was demonstrated on the example of surface plasmon polariton (SPP) modes in a single silver nanowire to achieve valley-dependent unidirectional transport of the excitonic emission and chiral Raman signals from a WS_2 multilayer.[26,27] Similar spatial separation and transport of the linear and nonlinear excitonic photons from monolayer WS_2 can also be realized with periodic nanostructures, including plasmonic metasurfaces[28–32] and photonic crystals[33,34]. While these hybrid systems have demonstrated extraordinary directionality of chiral coupling, the overall signal intensity and valley-locked transport distance are limited due to the use of TMDC multilayers and plasmonic nanostructures. On the one hand, the photoluminescence (PL) quantum yield of TMDC multilayers is typically orders of magnitude smaller than that of TMDC monolayers[35] (although the degree of valley polarization of the former is about 2-3 times larger than the latter[36]). The SPP modes in metal nanowires and plasmonic metasurfaces have a limited propagation length, typically about a few micrometers, due to the presence of the intrinsic Ohmic loss (typically ~0.4 dB/μm for the SPP modes).[37] It should be noted that the physical mechanism governing the selective coupling and unidirectional transport of the linear valley photons in the monolayer-TMDCs-loaded interfaces[28-33] remains elusive because the intrinsic valley polarization degree of the monolayer TMDCs at room temperature is almost zero. This has twofold implications: either valley polarization may not have played an essential role in the reported observations (especially since the coupling of quantum emitters without valley contrast with an SOI photonic crystal has been recently demonstrated[34]) or we are lacking theoretical understanding of the tagging of an valley excitonic state to the in-plane momentum of the plasmonic optical spin-orbit mode, as was pointed out in Ref. 30.

In this article, we develop an explainable chiral valley-photonic interface consisting of a silica microfiber coupled to a WS_2 monolayer to realize spatial separation and long-distance transport of emission from different valleys, based on the valley-polarized trion emission. In a WS_2 monolayer, trions provide significant valley polarization degree together with high PL intensity at room temperature, outperforming neutral excitons in WS_2 multilayers. Compared to plasmonic realisations[26,27,30,31], the proposed configuration presents several remarkable advantages, including the propagation distance of more than 10^4 times longer, practically limited by the length of the microfiber (propagation loss in a microfiber is ~10^{-5} dB/μm)[37], and a significantly larger signal intensity. Not only the excitation polarisation but also the position with respect to the fiber can be used to route the trion emission in different directions, providing also spatial selectivity of the emission in addition to spin selectivity. The use of robust microfiber technology makes the developed approach suitable for a wide range of practical device applications such as chiral molecule sensors, optical circulators, optical switches, CNOT quantum gates and complex spin optical networks.[38–42]

RESULTS AND DISCUSSION

Design and characterization of chiral valley-photonic interface. The proposed chiral valley-photonic interface consists of a WS_2 monolayer sandwiched between an MgF_2 substrate and a cleaved silica microfiber of 70 μm in length and 1 μm in diameter (Fig. 1a). The refractive index of MgF_2 (~1.38) is lower than that of silica (~1.45), ensuring good confinement of light in the microfiber. Depending on the handedness (σ^+ and σ^-) of a near-resonant (593.5 nm) circularly polarized illumination, valley-dependent circularly polarized photoluminescence (CPL) can be generated from monolayer WS_2 at either +K or -K valley.[8,9] This CPL obeys the valley-dependent optical selection rules determined by the inversion symmetry breaking of the monolayer hexagonal lattice and the strong spin-orbit coupling in WS_2 (Fig. 1b).[43] The degree of valley polarization can be quantified by $P_v = (I_{+K}-I_{-K})/(I_{+K}+I_{-K})$, where I_{+K} and I_{-K} represent the CPL signal intensities from the two valleys (under $\sigma^{\pm}$-handedness excitation), respectively. Under the near-resonant excitation at room temperature, charged trions have a higher degree of valley polarization (0.3) under high-intensity excitation than neutral excitons (0.1) under low-intensity excitation in a monolayer WS_2 (Fig. S1),[18,26,44] arising from reduced trion intervalley scattering rate compare with that of neutral exciton.[45] As a result, to achieve a higher P_v, exciton-to-trion conversion is required. Using MgF_2 as the substrate makes the trions contribution to the valley pseudospins dominant, because a low-permittivity dielectric environment suppresses the radiative recombination rate of excitons more efficiently than trions.[46,47] Together with the photon-doping effect induced by a high power excitation, the polarization-resolved CPL spectra of the WS_2 monolayer (Fig. 1c) show trion-dominant emission peaks while a degree of valley polarization P_v about 0.3 is achieved. The nature of this trion emission at 630 nm is confirmed by the significant spectral separation from the neutral exciton emission by 46 meV and the red-shifted emission energy with increasing excitation intensity (Fig. S1).[48,49] Importantly, the WS_2 monolayer has robust trion-dominant valley polarization and a higher CPL intensity than the excitons in WS_2 multilayers (Fig. S2).[50,51]

In this context, optically generated valley excitons or trions, which can be modelled as circularly polarized electric dipoles, can locally couple to the microfiber modes with the local transverse SAM of the same handedness, and thus selected valley information can be directionally transported to a defined terminal of the microfiber via spin-momentum locking. Consequently, one can observe remarkably different PL signal intensities (denoted as I_L and I_R) at the left and right ends of the microfiber when the excitation beam is focused at either side of the microfiber, i.e., under off-centre illumination. Under the illumination through the fiber, the PL emission is coupled in both directions simultaneously, irrespective of the emission handedness. The upper panel of Fig. 1d shows the bright-field microscopy image of our hybrid interface, and the lower panel shows the same structure under laser excitation at 593.5 nm, exhibiting pronounced PL scattering at the ends of the microfiber. The measured spectrum of the scattered PL signal shows a trion-dominant emission peak at around 630 nm (Fig. S3), confirming efficient coupling of the trion emission to the guided modes.

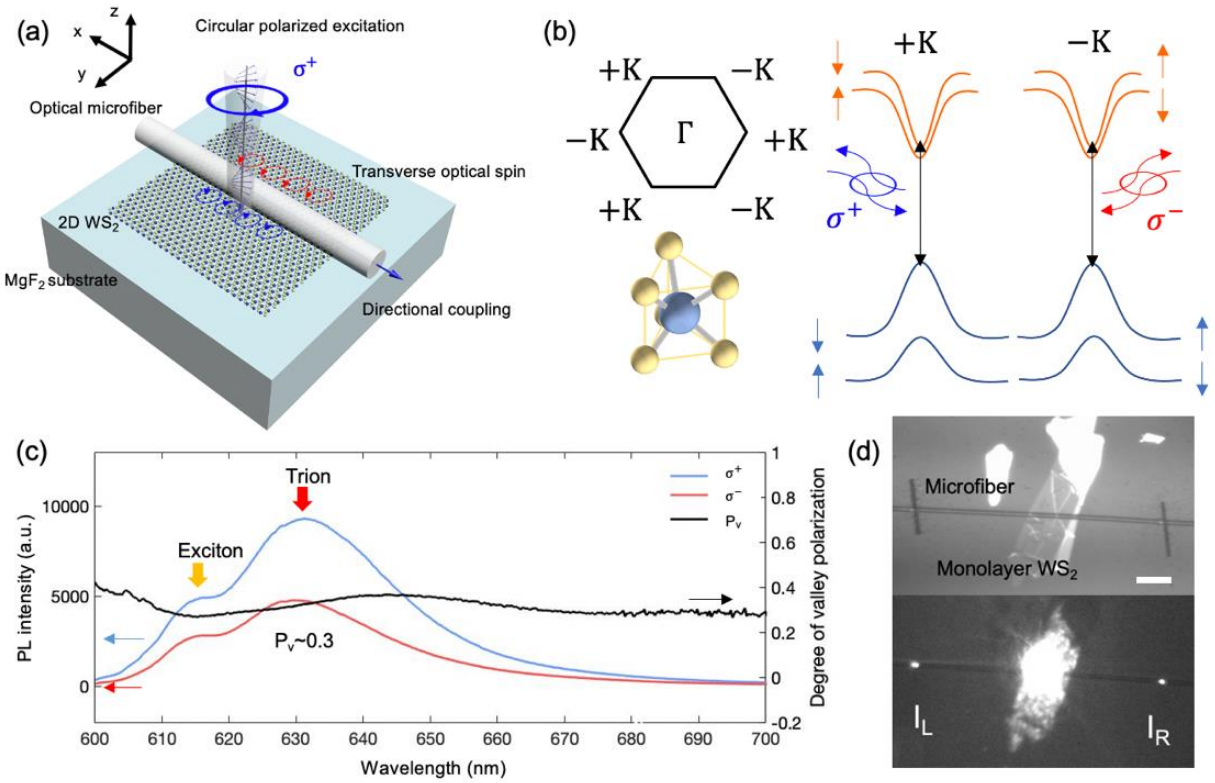

Figure 1. Valley-dependent directional coupling of trion emission to microfiber modes. (a) Schematic of a WS_2 monolayer supported on an MgF_2 substrate with a microfiber placed on top for directional separation of the valley trion emission. (b) Schematic of the valley-dependent selection rules for trion emission in a monolayer WS_2. The valley-dependent optical selection rules determined by the inversion symmetry breaking of the monolayer hexagonal lattice and the strong spin-orbit coupling in WS_2. (c) Polarization-resolved PL spectra of a WS_2 monolayer under the RCP (σ^+) excitation (red and blue lines), showing the exciton and trion emission peaks with a degree of valley polarization P_v of around 0.3 (black line). (d) Upper: bright-field microscopy image of the sample (scale bar 10 μm); Lower: the same sample area as the upper image under the 593.5 nm circularly-polarized excitation focused at the centre of a microfiber.

Microfiber mode analysis. To uncover the physical mechanism behind the pronounced spin-momentum locking effect in our hybrid valley-photonic interface, we first undertake numerical simulations based on the three-dimensional finite-difference time-domain (FDTD) method with finite-difference eigenmode (FDE) solver. An excited trion in WS_2 was modelled as a left/right-handed circular dipole by superposing two orthogonal linear dipoles with a phase difference $\pm\pi/2$. By changing the transverse location of the dipole with respect to the fiber at the z=0 interface, corresponding to the WS_2 monolayer, guide modes with defined propagating directions can be excited in the microfiber.

The electric field distribution profiles of the three dominant guided modes in the microfiber under circularly polarized dipole excitation are shown in Figs. 2a-c and S4. The fields in the fiber are mainly contributed by the LP_{01} and LP_{11} modes. In particular, the modes LP_{01y} and LP_{11y} play a major role since their electric fields match that of the circular dipole, that is, their dominant transverse electric (TE) polarization components in the *y* direction are consistent with the polarization of the circular dipole in the *x*-*y* plane. On the contrary, the modes with dominant TE polarization components along the *z* direction appear dark under the circular dipole excitation because their electric fields are perpendicular to the polarization of the circular dipole in the *x*-*y* plane (Fig. S5). The density of the transverse SAM associated with the guided modes can be characterized by a local Stokes parameter $S_3 = -2\mathrm{Im}(E_xE_y^*)/(|E_x|^2+|E_y|^2)$ in the *x*-*y* plane (Figs. 2d-f). Clearly, opposite spins appear at the microfiber surfaces along the *y* direction, and the value of S_3 approaches near-unity at the left and right surfaces ($y = \pm0.5$ μm, $z = 0.5$ μm) and zero at the top and bottom surfaces ($y = 0$ μm, $z = 0$ and 1.0 μm). At the $z = 0$ plane, where the circular dipole is placed, S_3 decreases to about 0.5 due to the presence of the substrate that tailors the local electric field profile. Interestingly, the spin associated with the LP_{11} mode flips inside the microfiber (Fig. 2f), which is attributed to the field distribution of the higher-order mode that can be regarded as a combination of two LP_{01y} modes.

The coupling efficiency for different modes varies when sweeping the location of circular dipole. When the circular dipole is located off the fiber centre along the transverse (*y*) direction at y = ±0.5 μm (Fig. 2g and h), 'wiggly' patterns in the field profiles appear due to multimode interference, whereas modes $LP_{11y,1}$ and $LP_{11y,2}$ are dominating.[52] As expected, the electric field exhibits an asymmetric distribution profile along the microfiber, leading to different field amplitudes at the fiber ends: $E_L > E_R$ in Fig. 2g and $E_L < E_R$ in Fig. 2h.

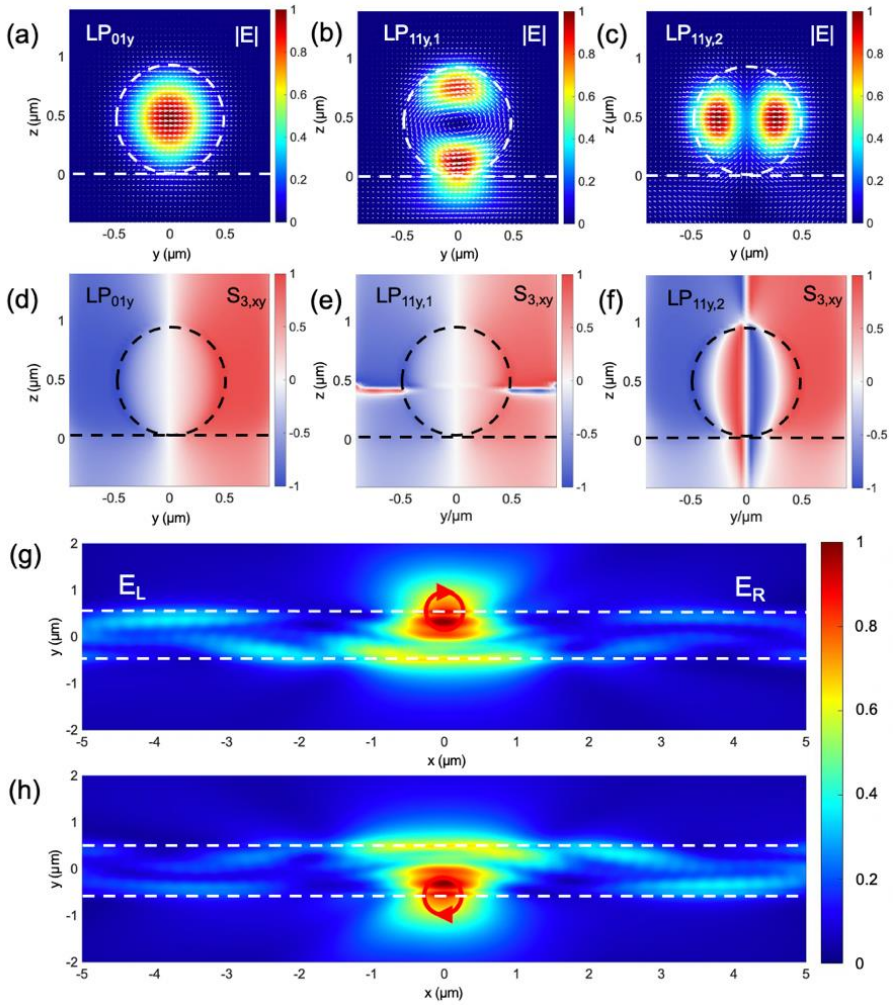

Figure 2. Mode analysis of a silica microfiber (70 μm long, 1 μm diameter) at 630 nm. (a-c) Electric-field intensity distribution profiles and electric field vectors (white arrows) of three guided modes excited by a circular dipole and (d-f) the corresponding local Stokes parameter S_3. Dashed lines outline the microfiber and the substrate. Note that the subscript "*y*" for the three LP modes indicate their near-unity TE polarization along the *y* direction. (g, h) Directional coupling of the radiation from a circular dipole at z = 0 at (g) y = +0.5 μm and (h) y = -0.5 μm to the guided modes of a nearby microfiber through the spin-momentum locking effect. The colour bar indicates the electric field amplitude in the longitudinal cross section of the microfiber (at z = 0.5 μm).

Valley-to-path directionality mapping. To quantify the valley-to-path directional coupling, we determine the coupling directionality of the hybrid interface by monitoring the transmitted intensity at the left and right ends of the fiber, denoted as T_L and T_R. The spin-momentum locking effect leads to a valley-to-path directionality parameter, defined as $D_0 = (T_L - T_R)/(T_L + T_R)$, which is influenced by both the spectral and spatial profiles of the trions emission. By displacing the circular dipole along the *y* direction, the wavelength- and location-dependent valley-to-path directionality $D_0(x, y, \lambda)$ can be calculated for the finite long fiber under study and a broad trion emission peak. It should be noted that the x-dependence of the directionality arises due to the reflection from the fiber ends and can be eliminated by using an optimised out-coupling from the microfiber. The contour plots in Figs. 3a and b show the calculated D_0 at x = 0 μm and λ = 630 nm, respectively, with the values exhibiting a strong dependence on either wavelength or the x coordinate. Note that the periodic variation in D_0 with wavelength (Fig. 3a) originates from the Fabry-Perot resonances in the microfiber of a finite length (the results for an infinite long microfiber shown in Figs. S6a and b have no such pattern). We find the local directionalities ($D_0 \sim \pm 0.47$) in Figs. 3a and b match well the density of a transverse SAM, i.e. the S_3 parameters of the microfiber multimodes, in Figs. 2d-f, as should be expected.[26] When the dipole is placed at z = 0.5 μm, the directionality approaches unity (Fig. S7), which agrees with the near-unity density of the local transverse SAM. To describe the directional coupling process, merely calculating the directionality is inadequate: a high coupling strength of the circular dipole to the multimode microfiber is also important to achieve high coupling efficiency. Figures 3c and d show the normalized coupling strength defined as $K_{tot}(x, y, \lambda) = (T_L + T_R)/(T_L + T_R)_{max}$, where $T_L + T_R$ is the total intensity of light coupled into guide modes and the maximum $(T_L + T_R)_{max}$ occurs at around x = 0 μm and λ = 700 nm in our system. We can see from the results that the coupling strength varies with the dipole wavelength and location, and is significantly enhanced by the Fabry-Perot resonances in the finite long fiber, approaching unity (in sharp contrast the results in Figs. S6c and d). With consideration of the measured emission spectrum in Fig. 1c, integrating the wavelength-dependent coupling directionality in Fig. 3a gives rise to an 'S'-shape overall directionality, D_{dipole} (Fig. 3e); integrating the wavelength-dependent coupling strength preserves the maximum at y = 0.

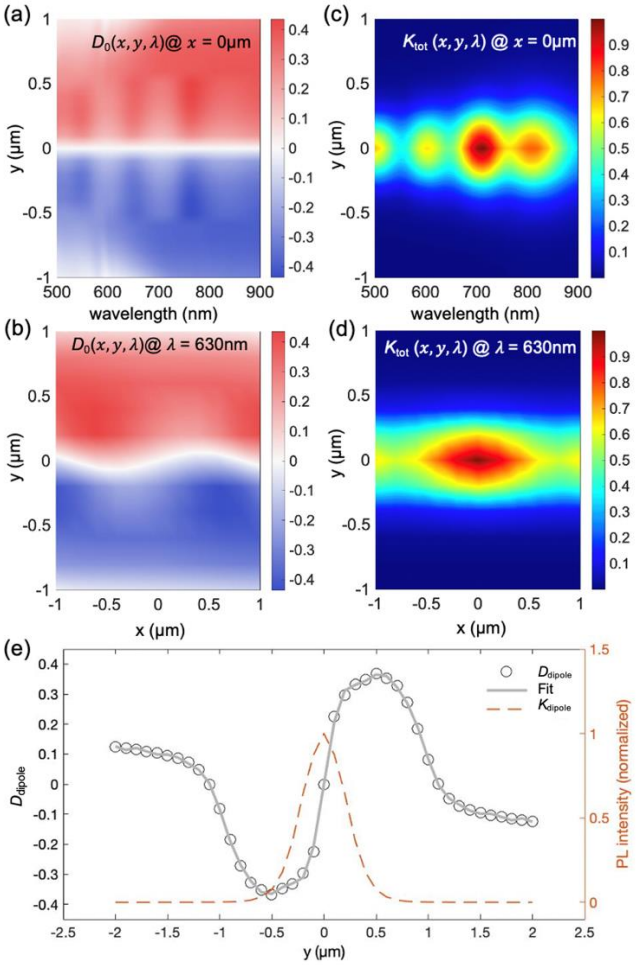

Figure 3. Contour plots of coupling directionality and coupling strength for the silica microfiber (70 μm long, 1 μm diameter) at x = 0 μm and λ = 630 nm. (a) Valley-to-path directionality D_0 and (c) normalized coupling strength K_{tot} as a function of the circular dipole wavelength and position along the y axis at x = 0 μm. Spatial mappings of (b) D_0 and (d) K_{tot} at 630 nm. (e) Wavelength-integrated coupling directionality D_{dipole} (grey dots) and coupling strength (dashed orange line), K_{dipole}, by considering the emission spectrum of monolayer WS_2 in Fig. 1c. The solid line is a guide to the eye.

Measurement of directional emission. In the experiment, a focused circular polarized laser beam was displaced transversely across the microfiber and the PL intensities at the left and right ends of the fiber were measured. The experimental overall directionality of the valley trion-dominant emissions to the microfiber multimodes can be determined as $K_{exp} = (I_L - I_R)/(I_L + I_R)$ (Figs. 4a-d). Note that the PL intensity at each end was obtained by deducting the average grey value of a background area next to the end from the maximum grey value of the scattering spot (data analysis and corresponding results are shown in Fig. S8). Note that in the raw data of Figs. 4a-d, the right ends always have larger scattering peak intensities than the left ends, and both ends have smaller intensities when the excitation beam is located at the upper side. These effects are caused by various experimental factors, such as the off-centre excitation along the longitudinal direction and unequal scattering efficiency of the microfiber ends (due to different end facets), leading to an offset of -0.35 in the overall directionality as determined from the results in Fig. S9. After subtracting this offset from raw data, the observed directionality, $K_{exp}(y)$ varies in an "S" shape manner within the range of ± 0.1 (Fig. 4e). Under the opposite circular polarized illumination, the $K_{exp}(y)$ curve flips (Fig. 4f), with approximately the same directionality variation. This is an illustration and consequence of the flipping of transverse SAM associated with the microfiber guide modes on the opposite sides across the fiber. This conclusion is further confirmed by the results for a linear polarized excitation: no directional emission occurs with a nearly zero $K_{exp}(y)$ (Fig. 4g). Noticeably, remarkable directional emissions with similar features as Figs. 4e and f are also observed on microfibers with diameters as large as 2 μm and 1.5 μm (Section 6 in supporting information). Despite the increased number of modes in the thicker microfibers, the spin-valley interfaces preserve the maximum overall directionality of about 0.1, demonstrating excellent robustness in the directional emission. We note that the distances between the dip and peak values of K_{exp} in Figs. 4e and f are larger than the microfiber diameter 1 μm, which is due to the finite size of excitation spot on WS_2 and exciton diffusion, consistent with the previous work[26]. The dashed orange lines in Figs. 4e-g show the normalized total PL intensity, $I_{tot} = I_L + I_R$, where the dips at around y = 0 is due to the fact that the scattering effect of the microfiber screens the laser-WS_2 interaction strength. However, such screening has little influence in the valley polarization of WS_2 at around y = ±0.5 μm.

To understand the difference between the calculated directionality and the slightly reduced experimental overall directionality, we develop a semi-experimental, semi-analytical model (Section 7 in supporting information) by considering many experimental factors, including (1) measured degree of valley polarization, (2) chiral PL spectral profile, (3) finite size of excitation spot and exciton diffusion, (4) off-centre longitudinal location of excitation spot, (5) off-axis transverse scanning with respect to the microfiber, and (6) unequal scattering efficiencies of the two fiber ends. Results for an ideal interface and our experimental interface are compared by integrating the calculated valley-to-path directionality $D_0(x,y,\lambda)$ and normalized coupling strength $K_{tot}(x,y,\lambda)$ with respect to the degree of valley polarization P_V and the experimental spectral and spatial profiles of PL emission $I_{PL}(x,y,\lambda)$: $K_{exp}(y) = \frac{[D_0 K_{tot} P_V] \otimes I_{PL}}{[K_{tot} + 2K^{other}] \otimes I_{PL}}$,[26] where K^{other} denotes the efficiency of bidirectional coupled PL emission via achiral coupling channels. With such treatment, we obtain an excellent agreement between the experimental data and the theoretical fit given by the above equation in Figs. 4e and f. We also extract from the fit an experimental data of $K^{other} < 0.2\%$, indicating that most of the valley photons are coupled into the microfiber guided modes via the spin-momentum locking effect with an efficiency of chiral coupling $K_{chiral\ coupling} = 1 - 2K^{other}$ over 99.6%. In the meanwhile, an experimental valley-to-path directionality D_{exp} can be obtained by: $D_{exp}(y) = \frac{K_{exp}(y)/P_V}{1 - 2K^{other}/(I_{tot}(y) K_{coupling})}$, where $K_{exp}(y)$ and $I_{tot}(y)$ are the experimental overall directionality and normalized total PL intensity, respectively. $K_{coupling}$ is the coupling efficiency of our interface, defined as $\frac{I_L + I_R}{I_{PL}}$, which is measured to be about 6.6% in our system. Thus, we have realized a room-temperature chiral interface coupling the valley trion-associated pseudospins of monolayer WS_2 and the momentum direction of the microfiber modes, with a fidelity D_{exp} as high as ± 0.38.

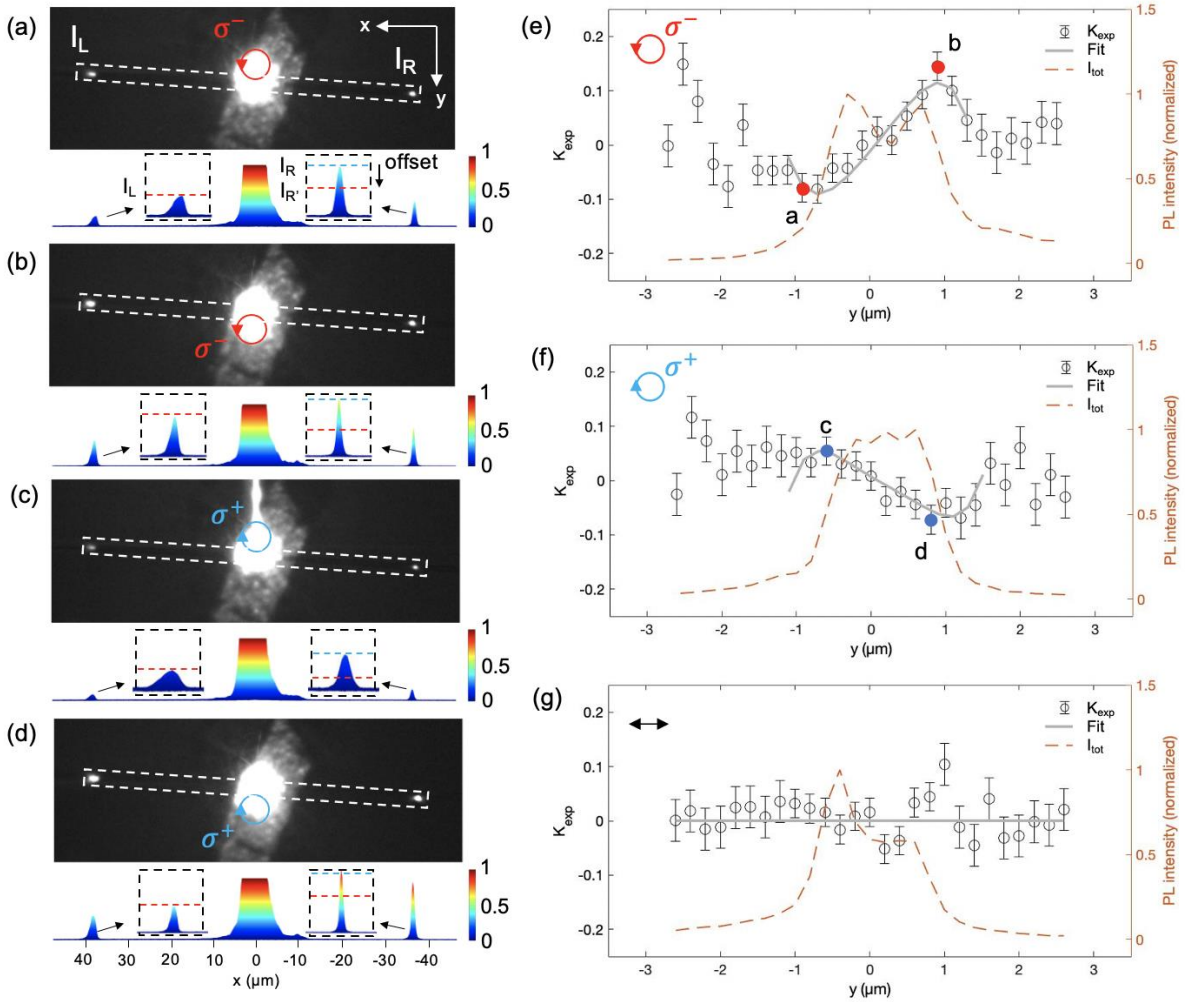

Figure 4. Experimental demonstration of valley-dependent directional emission. (a-d) Upper panels are the greyscale images of the hybrid interface under 593.5 nm circularly polarized laser excitation at the two transverse sides of the fiber. The white dashed lines in each panel outline the microfiber. Lower panels plot corresponding greyscale values along the microfiber, giving the raw scattering intensities at the centre and two ends of the fiber. Deducting an offset of -0.35 from the raw intensity of each right end (labelled by the dashed blue line) gives the actual directional emission intensity (labelled by the dashed red line). Directional coupling can be clearly observed from the heights of the red dashed lines. (e-g) Overall directionality K_{exp} (circles with error bars) and normalized total PL intensity I_{tot} under σ^-, σ^+ and linear polarized excitation as a function of illumination position in the y direction. Grey lines are theoretical fits to the experimental data. Data points labelled as "a, b, c, d" in (e) and (f) were extracted from Figs. 4a-d.

CONCLUSION

In conclusion, we have demonstrated chiral coupling of valley trions-dominant pseudospins in monolayer WS_2 and microfiber multimodes via the transverse SAM of guided modes. The directional emission with high intensities at both ends of a microfiber has been observed. Compared with similar interfaces based on metallic nanowires and multilayers WS_2 valley excitons, the proposed valley interface, using trions and microfibers, provides much higher signal intensity, orders of magnitude larger longer propagation range and preserves at the same time high degree of the valley emission separation (Section 8 in supporting information). The proposed interface can be applied in valleytronics and novel optical systems such as optical circulators, chiral molecules detectors, and chiral quantum spin networks, providing a promising platform for the research of spin-photonics.

METHODS

Sample preparation. Few-layered WS_2 flakes were mechanically exfoliated from a single WS_2 crystal onto a scotch tape and then were adhered onto an MgF_2 substrate through PDMS film or viscoelastic stamping. The layers of WS_2 were identified by contrast ratio in customized optical microscope (Olympus BX 51) and its PL signal. The microfibers were fabricated from the standard single mode fiber using the flame brushing method. The fiber was heated in a hydrogen flame and became soft, and two step-motors pulled it continuously. All the microfibers were tested with transmission loss less than 1 dB at 1550 nm. They were transferred to WS_2 specimen by a homemade *x-y-z* micro-movement stage under observation of optical microscope. Lastly, a femtosecond laser-based fabrication system (Newport femtoFBG) was used to cut the microfiber of about 70 μm in length (within the limited field of view of a 100× objective).

Experimental measurement. Samples were mounted onto a nano-positioning stage (Physik Instrumente P-563.3CD PIMarsTM) with 0.5 nm step resolution to allow raster scanning along the transverse direction of the microfiber with a step of 200nm. A 593.5 nm CW laser was used to illuminate the sample, and its circular polarization state was controlled by a pair of half waveplate and quarter waveplate (installed in a cage system) placed after the laser source. A confocal microscope with a 100× dry objective (Olympus, NA = 0.8) and a 50/50 beam splitter was used to focus and collect the incident light onto and, the light emission from, the sample. The excitation spot is measured to be Gaussian distribution with a diameter of 2μm and a power density of around 400mW/μm^2. A TE-cooled CCD (Pixis: 400 BR eXcelon) mounted on standard spectrometer (Princeton Instrument, SP2500i, 150 l/mm grating) was used to analyze the signal, before which a 600 nm long-pass filter was inserted to block the excitation laser. The integration time of signal collection in our experiments was 2 sec. To investigate the degree of valley polarization in WS_2, a quarter waveplate and a polarizer were placed after the microscope to resolve the CPL signals.

Electromagnetic simulation. Lumerical FDTD solution was used to numerically investigate directional emission of the valley exciton (Figs. 2g and h) and quantitatively calculate the valley-to-path directionality (Fig. 3) of the hybrid interface. In our simulation, a circular dipole is placed between the MgF_2 substrate and the microfiber to model valley excitons. Left/right-handed circular dipoles are created by superposing two orthogonal linear polarized dipoles with a $\pm\pi/2$ phase difference. The refractive index of materials used are Palik database for silica and Dodge 1984 database for MgF_2. A pair of monitors are used to calculate the transmission at the two fiber ends. The FDE solver from Lumerical was used to calculate eigenmodes of the microfibers and corresponding local Stokes parameters (Figs. 2a-f) and also determine bright and dark modes based on the beam profiles recorded by the FDTD monitors.

ASSOCIATED CONTENT

The supporting information is available free of charge via the Internet at http://pubs.acs.org.

Fig.S1. Power dependence of trion emission intensity and valley polarization, Fig.S2. Layers dependence of trion emission intensity and valley polarization, Fig.S3. Spectral visualization of trion emission coupled in microfiber, Fig.S4. Schematic diagram of vector modes and corresponding scalar modes in 1 μm diameter microfiber, Fig.S5. Dark modes in 1 μm diameter microfiber, Fig.S6. Contour plots of coupling directionality and coupling strength for the silica microfiber (infinite long, 1 μm diameter) at x = 0 μm and λ = 630 nm, Fig.S7. Contour plots of coupling directionality for the silica microfiber (infinite long, 1 μm diameter) at x = 0.5 μm, Fig.S8. Results of K_{exp} and I_{tot} obtained by another data grabbing methods, Fig.S9. Demonstration of the offset in raw directionality of valley polarized PL as a function of the transverse position of excitation along the microfiber, Fig.S10. Experimental directionality and normalized total PL intensity for interfaces with thicker microfiber, Fig.S11. Multimodes in thicker microfiber, Fig.S12. Spatial profile $I_{PL}(x, y)$ of PL emission from monolayer WS_2, Table S1. Comparing the properties of hybrid WS_2 multilayers-nanowire system and our interface.

AUTHOR INFORMATION

Corresponding Author

Dangyuan Lei - Department of Materials Science and Engineering, The City University of Hong Kong, Hong Kong 999077, China; Email: dangylei@cityu.edu.hk

Authors

Pei-Gang Chen - Department of Materials Science and Engineering, The City University of Hong Kong, Hong Kong 999077, China

Zhiyong Li - Department of Applied Biology and Chemical Technology, The Hong Kong Polytechnic University, Hong Kong 999077, China

Yun Qi - Department of Electrical Engineering, The Hong Kong Polytechnic University, Hong Kong 999077, China

Tsz Wing Lo - Department of Materials Science and Engineering, The City University of Hong Kong, Hong Kong 999077, China

Shubo Wang - Department of Physics, City University of Hong Kong, Hong Kong 999077, China

Wei Jin - Department of Electrical Engineering, The Hong Kong Polytechnic University, Hong Kong 999077, China

Shanhui Fan - Department of Electrical Engineering and Ginzton Laboratory, Stanford University, Stanford, CA 94305-4088, USA

Anatoly V. Zayats - Department of Physics and London Centre for Nanotechnology, King's College London, Strand, London, WC2R 2LS, UK

Complete contact information is available at: http://pubs.acs.org.

Author Contributions

The manuscript was written through contributions of all authors.

Funding Sources

Research Grants Council of Hong Kong (AoE/P-701/20); the City University of Hong Kong (APRC Grant No. 9610456); the U. S. Office of Naval Research (Grant No. N00014-20-1-2450); the UK Engineering and Physical Sciences Research Council; the European Research Council iCOMM project 789340.

Notes

The authors declare no conflicts of interest.

ACKNOWLEDGMENT

P. G. C. thanks Dr. Xiaolin Chen for the useful discussion on numerical calculations.

REFERENCES

(1) Rycerz, A.; Tworzydło, J.; Beenakker, C. W. J. Valley Filter and Valley Valve in Graphene. *Nat. Phys.* **2007**, *3* (3), 172–175. https://doi.org/10.1038/nphys547.

(2) Yao, W.; Xiao, D.; Niu, Q. Valley-Dependent Optoelectronics from Inversion Symmetry Breaking. *Phys. Rev. B* **2008**, *77* (23), 235406. https://doi.org/10.1103/PhysRevB.77.235406.

(3) Shkolnikov, Y. P.; De Poortere, E. P.; Tutuc, E.; Shayegan, M. Valley Splitting of AlAs Two-Dimensional Electrons in a Perpendicular Magnetic Field. *Phys. Rev. Lett.* **2002**, *89* (22), 226805. https://doi.org/10.1103/PhysRevLett.89.226805.

(4) Gunawan, O.; Shkolnikov, Y. P.; Vakili, K.; Gokmen, T.; De Poortere, E. P.; Shayegan, M. Valley Susceptibility of an Interacting Two-Dimensional Electron System. *Phys. Rev. Lett.* **2006**, *97* (18), 186404. https://doi.org/10.1103/PhysRevLett.97.186404.

(5) Xiao, D.; Yao, W.; Niu, Q. Valley-Contrasting Physics in Graphene: Magnetic Moment and Topological Transport. *Phys. Rev. Lett.* **2007**, *99* (23), 236809. https://doi.org/10.1103/PhysRevLett.99.236809.

(6) Gunawan, O.; Habib, B.; De Poortere, E. P.; Shayegan, M. Quantized Conductance in an AlAs Two-Dimensional Electron System Quantum Point Contact. *Phys. Rev. B* **2006**, *74* (15), 155436. https://doi.org/10.1103/PhysRevB.74.155436.

(7) You, Y.; Zhang, X.-X. X.; Berkelbach, T. C.; Hybertsen, M. S.; Reichman, D. R.; Heinz, T. F. Observation of Biexcitons in Monolayer WSe_2. *Nat. Phys.* **2015**, *11* (6), 477–481. https://doi.org/10.1038/nphys3324.

(8) Zeng, H.; Dai, J.; Yao, W.; Xiao, D.; Cui, X. Valley Polarization in MoS_2 Monolayers by Optical Pumping. *Nat. Nanotechnol.* **2012**, *7* (8), 490–493. https://doi.org/10.1038/nnano.2012.95.

(9) Mak, K. F.; He, K.; Shan, J.; Heinz, T. F. Control of Valley Polarization in Monolayer MoS_2 by Optical Helicity. *Nat. Nanotechnol.* **2012**, *7* (8), 494–498. https://doi.org/10.1038/nnano.2012.96.

(10) Mak, K. F.; He, K.; Lee, C.; Lee, G. H.; Hone, J.; Heinz, T. F.; Shan, J. Tightly Bound Trions in Monolayer MoS_2. *Nat. Mater.* **2013**, *12* (3), 207–211. https://doi.org/10.1038/nmat3505.

(11) Xiao, J.; Ye, Z.; Wang, Y.; Zhu, H.; Wang, Y.; Zhang, X. Nonlinear Optical Selection Rule Based on Valley-Exciton Locking in Monolayer WS_2. *Light Sci. Appl.* **2015**, *4* (12), e366--e366. https://doi.org/10.1038/lsa.2015.139.

(12) Shomroni, I.; Rosenblum, S.; Lovsky, Y.; Bechler, O.; Guendelman, G.; Dayan, B. All-Optical Routing of Single Photons by a One-Atom Switch Controlled by a Single Photon. *Science.* **2014**, *345* (6199), 903–906. https://doi.org/10.1126/science.1254699.

(13) Mitsch, R.; Sayrin, C.; Albrecht, B.; Schneeweiss, P.; Rauschenbeutel, A. Quantum State-Controlled Directional Spontaneous Emission of Photons into a Nanophotonic Waveguide. *Nat. Commun.* **2014**, *5* (1), 5713. https://doi.org/10.1038/ncomms6713.

(14) Petersen, J.; Volz, J.; Rauschenbeutel, A. Chiral Nanophotonic Waveguide Interface Based on Spin-Orbit Interaction of Light. *Science.* **2014**, *346* (6205), 67–71. https://doi.org/10.1126/science.1257671.

(15) Sayrin, C.; Junge, C.; Mitsch, R.; Albrecht, B.; O'Shea, D.; Schneeweiss, P.; Volz, J.; Rauschenbeutel, A.; O'Shea, D.; Schneeweiss, P.; Volz, J.; Rauschenbeutel, A. Nanophotonic Optical Isolator Controlled by the Internal State of Cold Atoms. *Phys. Rev. X* **2015**, *5* (4), 41036. https://doi.org/10.1103/PhysRevX.5.041036.

(16) Coles, R. J.; Price, D. M.; Dixon, J. E.; Royall, B.; Clarke, E.; Kok, P.; Skolnick, M. S.; Fox, A. M.; Makhonin, M. N. Chirality of Nanophotonic Waveguide with Embedded Quantum Emitter for Unidirectional Spin Transfer. *Nat. Commun.* **2016**, *7* (1), 11183. https://doi.org/10.1038/ncomms11183.

(17) Rothe, M.; Zhao, Y.; Müller, J.; Kewes, G.; Koch, C. T.; Lu, Y.; Benson, O. Self-Assembly of Plasmonic Nanoantenna–Waveguide Structures for Subdiffractional Chiral Sensing. *ACS Nano* **2021**, *15* (1), 351–361. https://doi.org/10.1021/acsnano.0c05240.

(18) Chen, P.; Lo, T. W.; Fan, Y.; Wang, S.; Huang, H.; Lei, D. Chiral Coupling of Valley Excitons and Light through Photonic Spin–Orbit Interactions. *Adv. Opt. Mater.* **2020**, *8* (5), 1901233. https://doi.org/10.1002/adom.201901233.

(19) Bliokh, K. Y.; Rodríguez-Fortuño, F. J.; Nori, F.; Zayats, A. V. Spin–Orbit Interactions of Light. *Nat. Photonics* **2015**, *9* (12), 796–808. https://doi.org/10.1038/nphoton.2015.201.

(20) Shi, P.; Du, L.; Li, C.; Zayats, A. V.; Yuan, X. Transverse Spin Dynamics in Structured Electromagnetic Guided Waves. *Proc. Natl. Acad. Sci.* **2021**, *118* (6), e2018816118. https://doi.org/10.1073/pnas.2018816118.

(21) O'Connor, D.; Ginzburg, P.; Rodríguez-Fortuño, F. J.; Wurtz, G. A.; Zayats, A. V. Spin–Orbit Coupling in Surface Plasmon Scattering by Nanostructures. *Nat. Commun.* **2014**, *5* (1), 5327. https://doi.org/10.1038/ncomms6327.

(22) Rodriguez-Fortuno, F. J.; Marino, G.; Ginzburg, P.; O'Connor, D.; Martinez, A.; Wurtz, G. a; Zayats, A. V. Near-Field Interference for the Unidirectional Excitation of Electromagnetic Guided Modes. *Science.* **2013**, *340* (6130), 328–330. https://doi.org/10.1126/science.1233739.

(23) Bliokh, K. Y.; Nori, F. Transverse Spin of a Surface Polariton. *Phys. Rev. A* **2012**, *85* (6), 61801. https://doi.org/10.1103/PhysRevA.85.061801.

(24) Wang, S.; Hou, B.; Lu, W.; Chen, Y.; Zhang, Z. Q.; Chan, C. T. Arbitrary Order Exceptional Point Induced by Photonic Spin–Orbit Interaction in Coupled Resonators. *Nat. Commun.* **2019**, *10* (1), 832. https://doi.org/10.1038/s41467-019-08826-6.

(25) Eismann, J. S.; Nicholls, L. H.; Roth, D. J.; Alonso, M. A.; Banzer, P.; Rodríguez-Fortuño, F. J.; Zayats, A. V; Nori, F.; Bliokh, K. Y. Transverse Spinning of Unpolarized Light. *Nat. Photonics* **2021**, *15* (2), 156–161. https://doi.org/10.1038/s41566-020-00733-3.

(26) Gong, S.-H.; Alpeggiani, F.; Sciacca, B.; Garnett, E. C.; Kuipers, L. Nanoscale Chiral Valley-Photon Interface through Optical Spin-Orbit Coupling. *Science.* **2018**, *359* (6374), 443–447. https://doi.org/10.1126/science.aan8010.

(27) Guo, Q.; Fu, T.; Tang, J.; Pan, D.; Zhang, S.; Xu, H. Routing a Chiral Raman Signal Based on Spin-Orbit Interaction of Light. *Phys. Rev. Lett.* **2019**, *123* (18), 183903. https://doi.org/10.1103/PhysRevLett.123.183903.

(28) Chen, H.; Liu, M.; Xu, L.; Neshev, D. N. Valley-Selective Directional Emission from a Transition-Metal Dichalcogenide Monolayer Mediated by a Plasmonic Nanoantenna. *Beilstein J. Nanotechnol.* **2018**, *9* (1), 780–788. https://doi.org/10.3762/bjnano.9.71.

(29) Hu, G.; Hong, X.; Wang, K.; Wu, J.; Xu, H.-X.; Zhao, W.; Liu, W.; Zhang, S.; Garcia-Vidal, F.; Wang, B.; Lu, P.; Qiu, C.-W. Coherent Steering of Nonlinear Chiral Valley Photons with a Synthetic Au–WS_2 Metasurface. *Nat. Photonics* **2019**, *13* (7), 467–472. https://doi.org/10.1038/s41566-019-0399-1.

(30) Chervy, T.; Azzini, S.; Lorchat, E.; Wang, S.; Gorodetski, Y.; Hutchison, J. A.; Berciaud, S.; Ebbesen, T. W.; Genet, C. Room Temperature Chiral Coupling of Valley Excitons with Spin-Momentum Locked Surface Plasmons. *ACS Photonics* **2018**, *5* (4), 1281–1287. https://doi.org/10.1021/acsphotonics.7b01032.

(31) Sun, L.; Wang, C.-Y.; Krasnok, A.; Choi, J.; Shi, J.; Gomez-Diaz, J. S.; Zepeda, A.; Gwo, S.; Shih, C.-K.; Alù, A.; Li, X. Separation of Valley Excitons in a MoS_2 Monolayer Using a Subwavelength Asymmetric Groove Array. *Nat. Photonics* **2019**, *13* (3), 180–184. https://doi.org/10.1038/s41566-019-0348-z.

(32) Hong, X.; Hu, G.; Zhao, W.; Wang, K.; Sun, S.; Zhu, R.; Wu, J.; Liu, W.; Loh, K. P.; Wee, A. T. S.; Wang, B.; Alù, A.; Qiu, C.-W.; Lu, P. Structuring Nonlinear Wavefront Emitted from Monolayer Transition-Metal Dichalcogenides. *Research* **2020**, *2020*, 1–10. https://doi.org/10.34133/2020/9085782.

(33) Wang, J.; Li, H.; Ma, Y.; Zhao, M.; Liu, W.; Wang, B.; Wu, S.; Liu, X.; Shi, L.; Jiang, T.; Zi, J. Routing Valley Exciton Emission of a WS_2 Monolayer via Delocalized Bloch Modes of In-Plane Inversion-Symmetry-Broken Photonic Crystal Slabs. *Light*

Sci. Appl. **2020**, *9* (1), 148. https://doi.org/10.1038/s41377-020-00387-4.

(34) Rong, K.; Wang, B.; Reuven, A.; Maguid, E.; Cohn, B.; Kleiner, V.; Katznelson, S.; Koren, E.; Hasman, E. Photonic Rashba Effect from Quantum Emitters Mediated by a Berry-Phase Defective Photonic Crystal. *Nat. Nanotechnol.* **2020**, *15* (11), 927–933. https://doi.org/10.1038/s41565-020-0758-6.

(35) Splendiani, A.; Sun, L.; Zhang, Y.; Li, T.; Kim, J.; Chim, C.-Y.; Galli, G.; Wang, F. Emerging Photoluminescence in Monolayer MoS_2. *Nano Lett.* **2010**, *10* (4), 1271–1275. https://doi.org/10.1021/nl903868w.

(36) Su, H.; Wei, C.; Deng, A.; Deng, D.; Yang, C.; Dai, J.-F. Anomalous Enhancement of Valley Polarization in Multilayer WS_2 at Room Temperature. *Nanoscale* **2017**, *9* (16), 5148–5154. https://doi.org/10.1039/C7NR00554G.

(37) Guo, X.; Ying, Y.; Tong, L. Photonic Nanowires: From Subwavelength Waveguides to Optical Sensors. *Acc. Chem. Res.* **2014**, *47* (2), 656–666. https://doi.org/10.1021/ar400232h.

(38) Lodahl, P.; Mahmoodian, S.; Stobbe, S.; Rauschenbeutel, A.; Schneeweiss, P.; Volz, J.; Pichler, H.; Zoller, P. Chiral Quantum Optics. *Nature* **2017**, *541* (7638), 473–480. https://doi.org/10.1038/nature21037.

(39) Guo, X.; Qiu, M.; Bao, J.; Wiley, B. J.; Yang, Q.; Zhang, X.; Ma, Y.; Yu, H.; Tong, L. Direct Coupling of Plasmonic and Photonic Nanowires for Hybrid Nanophotonic Components and Circuits. *Nano Lett.* **2009**, *9* (12), 4515–4519. https://doi.org/10.1021/nl902860d.

(40) Cao, Z.; Gao, H.; Qiu, M.; Jin, W.; Deng, S.; Wong, K. K.; Lei, D. Chirality Transfer from Sub-Nanometer Biochemical Molecules to Sub-Micrometer Plasmonic Metastructures: Physiochemical Mechanisms, Biosensing, and Bioimaging Opportunities. *Adv. Mater.* **2020**, *32* (41), 1907151. https://doi.org/10.1002/adma.201907151.

(41) Qiu, M.; Zhang, L.; Tang, Z.; Jin, W.; Qiu, C.-W.; Lei, D. Y. 3D Metaphotonic Nanostructures with Intrinsic Chirality. *Adv. Funct. Mater.* **2018**, *28* (45), 1803147. https://doi.org/10.1002/adfm.201803147.

(42) Tan, P.-H.; Zhang, L.; Dai, L.; Zhou, S. Preface to the Special Issue on 2D-Materials-Related Physical Properties and Optoelectronic Devices. *J. Semicond.* **2019**, *40* (6), 060101. https://doi.org/10.1088/1674-4926/40/6/060101.

(43) Xu, X.; Yao, W.; Xiao, D.; Heinz, T. F. Spin and Pseudospins in Layered Transition Metal Dichalcogenides. *Nat. Phys.* **2014**, *10* (5), 343–350. https://doi.org/10.1038/nphys2942.

(44) Hanbicki, A. T.; Kioseoglou, G.; Currie, M.; Hellberg, C. S.; McCreary, K. M.; Friedman, A. L.; Jonker, B. T. Anomalous Temperature-Dependent Spin-Valley Polarization in Monolayer WS_2. *Sci. Rep.* **2016**, *6* (1), 18885. https://doi.org/10.1038/srep18885.

(45) Hao, K.; Xu, L.; Wu, F.; Nagler, P.; Tran, K.; Ma, X.; Schüller, C.; Korn, T.; MacDonald, A. H.; Moody, G.; Li, X. Trion Valley Coherence in Monolayer Semiconductors. *2D Mater.* **2017**, *4* (2), 025105. https://doi.org/10.1088/2053-1583/aa70f9.

(46) Lin, Y.; Ling, X.; Yu, L.; Huang, S.; Hsu, A. L.; Lee, Y. H.; Kong, J.; Dresselhaus, M. S.; Palacios, T. Dielectric Screening of Excitons and Trions in Single-Layer MoS_2. *Nano Lett.* **2014**, *14* (10), 5569–5576. https://doi.org/10.1021/nl501988y.

(47) Liang, F.; Xu, H.; Dong, Z.; Xie, Y.; Luo, C.; Xia, Y.; Zhang, J.; Wang, J.; Wu, X. Substrates and Interlayer Coupling Effects on $Mo_{1-x}W_xSe_2$ Alloys. *J. Semicond.* **2019**, *40* (6), 062005. https://doi.org/10.1088/1674-4926/40/6/062005.

(48) Berkelbach, T. C.; Hybertsen, M. S.; Reichman, D. R. Theory of Neutral and Charged Excitons in Monolayer Transition Metal Dichalcogenides. *Phys. Rev. B* **2013**, *88* (4), 45318. https://doi.org/10.1103/PhysRevB.88.045318.

(49) Lundt, N.; Cherotchenko, E.; Iff, O.; Fan, X.; Shen, Y.; Bigenwald, P.; Kavokin, A. V.; Höfling, S.; Schneider, C. The Interplay between Excitons and Trions in a Monolayer of MoSe 2. *Appl. Phys. Lett.* **2018**, *112* (3), 031107. https://doi.org/10.1063/1.5019177.

(50) Lien, D.-H.; Uddin, S. Z.; Yeh, M.; Amani, M.; Kim, H.; Ager, J. W.; Yablonovitch, E.; Javey, A. Electrical Suppression of All Nonradiative Recombination Pathways in Monolayer Semiconductors. *Science.* **2019**, *364* (6439), 468–471. https://doi.org/10.1126/science.aaw8053.

(51) Carmiggelt, J. J.; Borst, M.; van der Sar, T. Exciton-to-Trion Conversion as a Control Mechanism for Valley Polarization in Room-Temperature Monolayer WS_2. *Sci. Rep.* **2020**, *10* (1), 17389. https://doi.org/10.1038/s41598-020-74376-3.

(52) Gong, S.-H.; Komen, I.; Alpeggiani, F.; Kuipers, L. Nanoscale Optical Addressing of Valley Pseudospins through Transverse Optical Spin. *Nano Lett.* **2020**, *20* (6), 4410–4415. https://doi.org/10.1021/acs.nanolett.0c01173.

SYNOPSIS TOC